Memristors Based on (Zr, Hf, Nb, Ta, Mo, W) High-Entropy Oxides

Minhyung Ahn, Yongmo Park, Seung Hwan Lee, Sieun Chae, Jihang Lee, John T. Heron, Emmanouil Kioupakis, Wei D. Lu,* and Jamie D. Phillips*

Memristors have emerged as transformative devices to enable neuromorphic and in-memory computing, where success requires the identification and development of materials that can overcome challenges in retention and device variability. Here, high-entropy oxide composed of Zr, Hf, Nb, Ta, Mo, and W oxides is first demonstrated as a switching material for valence change memory. This multielement oxide material provides uniform distribution and higher concentration of oxygen vacancies, limiting the stochastic behavior in resistive switching. (Zr, Hf, Nb, Ta, Mo, W) high-entropy-oxide-based memristors manifest the "cocktail effect," exhibiting comparable retention with HfO_2- or Ta_2O_5-based memristors while also demonstrating the gradual conductance modulation observed in WO_3-based memristors. The electrical characterization of these high-entropy-oxide-based memristors demonstrates forming-free operation, low device and cycle variability, gradual conductance modulation, 6-bit operation, and long retention which are promising for neuromorphic applications.

1. Introduction

Memristors are non-volatile memory devices that offer advantages in high device density, ultra-low power, ease of fabrication, and large analog capacity,[1–3] as well as desirable functionalities for analog circuit elements,[4,5] and computing applications, including neuromorphic computing,[6–11] and in-memory computing.[12–14] Particularly, oxide-based memristors, or valence charge memory, whose resistivity states are determined by the oxygen vacancy distribution in a switching

medium,[15,16] have demonstrated successful integration into crossbar array structures with WO_x,[9] TaO_x/HfO_x,[10] TiO_2,[11] and Al_2O_3/TiO_{2-x}[17] However, memristor technology is still limited by variability, retention, reliability, and endurance issues, which are inherent in the random nature of ionic diffusion.[2] Here we suggest the use of high-entropy oxides (HEOs),[18] which are multi-metallic (five or more typically) oxide systems stabilized by increased mixing entropy, as a switching medium for memristors to overcome these challenges. HEOs are derived from high-entropy alloys (HEAs), which form stable single-phase solid solutions despite the different crystal structures of each element.[19] Depending on the atomic radius differences, HEAs can be in a crystalline or amorphous phase.[20,21] Recently, HEOs have displayed interesting material characteristics, including a colossal dielectric constant,[22] high Li-ion conductivity,[23,24] and low thermal conductivity.[15] HEO-based memristors offer an opportunity to engineer the oxygen vacancy migration through enhanced lattice distortion and sluggish diffusion effects.[25] Moreover, the ability of HEO materials to maintain charge neutrality when elements with different charge valences are mixed,[26] provides a means to generate a uniform distribution of oxygen vacancies,[23,27] and associated reduction in device variability.[28]

In this work, materials with six transition metals (Zr, Hf, Nb, Ta, Mo, W) were selected in order to combine the successful characteristics of HfO_2, Ta_2O_5, and WO_3 in memristors while using Zr, Nb, and Mo (elements one row higher in the periodic table) to stabilize the HEO system. WO_3-based memristors exhibit forming-free behavior and good incremental conductance modulation (analog), but the retention is poor due to the high mobility of oxygen vacancies.[29] In contrast, HfO_2-based memristors show good retention with abrupt conductance changes (digital) between on/off states.[30] Ta_2O_5-based memristors present moderate analog conductance changes and good retention, but with limited on/off ratios.[31] HEO systems using HfO_2, Ta_2O_5, and WO_3 as switching mediums are expected to combine the favorable properties of these transition-metal-oxide-based memristors while overcoming the drawbacks of binary materials through the "cocktail effect" and high entropy.[25]

Dr. M. Ahn, Y. Park, Dr. S. H. Lee, Prof. W. D. Lu, Prof. J. D. Phillips
Department of Electrical Engineering and Computer Science
University of Michigan
1301 Beal Avenue, Ann Arbor, MI 48109-2122, USA
E-mail: wluee@umich.edu; jphilli@udel.edu
S. Chae, Dr. J. Lee, Prof. J. T. Heron, Prof. E. Kioupakis
Department of Materials Science and Engineering
University of Michigan
2300 Hayward St, Ann Arbor, MI 48109-2117, USA
Prof. J. D. Phillips
Department of Electrical and Computer Engineering
University of Delaware
Newark, DE 19716, USA

The ORCID identification number(s) for the author(s) of this article can be found under https://doi.org/10.1002/aelm.202001258.

**ADVANCED
SCIENCE NEWS**
www.advancedsciencenews.com

**ADVANCED
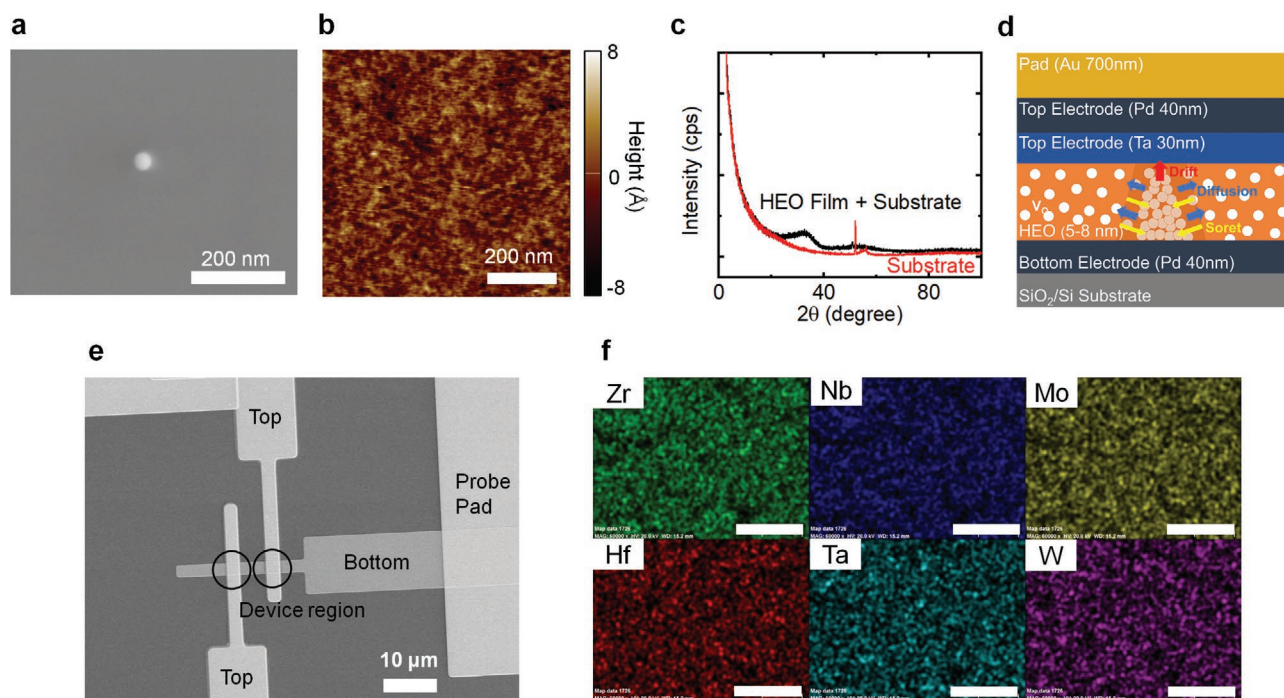ELECTRONIC
MATERIALS**
www.advelectronicmat.de

Figure 1. HEO thin film characterization for samples deposited in a vacuum. a) A SEM image HEO thin film. b) A height profile of AFM mapping. The film thickness is 4.5 nm. c) Grazing incidence XRD 2-theta spectra of a HEO thin film and a reference substrate. d) A device structure of HEO-based memristors. Ionic migration processes driving filament formation and disruption are illustrated in the schematic. e) A SEM image of a HEO-based memristor from a top view. f) EDS element mapping of HEO film. The white scale bar represents 300 nm.

2. Results

(Zr, Hf, Nb, Ta, Mo, W) HEO thin films were deposited by pulsed laser deposition (PLD) in an amorphous phase with varying oxygen partial pressure. The HEO thin films demonstrate a smooth surface morphology as shown in the SEM image of **Figure 1**a and atomic force microscopy (AFM) mapping in Figure 1b with 0.109 nm RMS surface roughness. The spherical particulate observed in Figure 1a is associated with the PLD deposition process. X-ray diffraction (XRD) results (Figure 1c) show a weak broad peak, suggesting that the deposited thin films are primarily amorphous. The small observed peak in the reference XRD scan is attributed to the (311) reflection of the (100) Si substrate commonly observed under grazing incidence conditions.[32,33] Energy-dispersive X-ray spectroscopy

(EDS) mapping (Figure 1f) confirms a homogeneous distribution of the six metal elements that are free of clustering, indicating a homogeneous solid solution.

The optical characteristics of the HEO thin films were investigated to gain insights into the electronic structure of the material. **Figure 2**a shows the absorption spectrum extracted from ellipsometry data using the relation, $\alpha = 4\pi\kappa/\lambda$, where α, κ, λ are the absorption coefficient, the imaginary part of refractive index (extinction coefficient), and the photon wavelength, respectively. The HEO films show broad optical absorption extending from the near-infrared to the ultraviolet spectral range. The optical band gap can be estimated by the Tauc relation $\alpha h\nu = A(h\nu - E_g)^n$, where $h\nu$, E_g, A, and n are respectively the photon energy, the optical band gap, a fitting constant prefactor, and the index representing the nature of interband
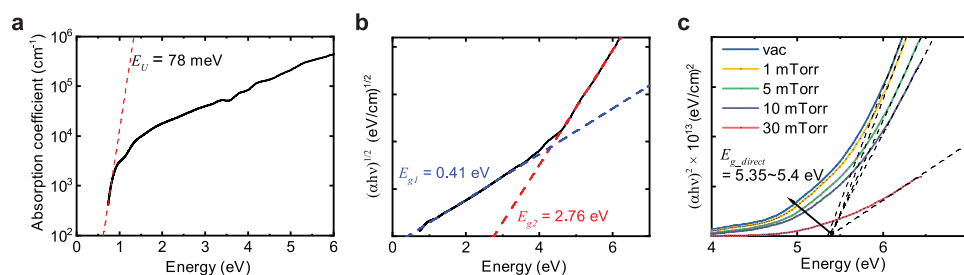

Figure 2. Optical characteristics of HEO thin film with Tauc and Urbach analysis. a) Absorption coefficient spectrum of HEO thin film deposited in a vacuum. The fitting line for Urbach energy and its value is inserted. b) An indirect Tauc plot using data from (a). c) Direct transition Tauc plots of HEO thin film deposited in different oxygen partial pressures. The linear trend lines for Tauc fittings and their extracted optical band gaps are inserted.

Table 1. Optical band gap and Urbach energy of the HEO thin film with varying oxygen partial pressure.

P_{O2} [mTorr]	E_{g1} [eV]	E_{g2} [eV]	E_U [meV]
Vacuum	0.41	2.76	78
1	0.47	2.84	78
5	0.56	2.86	77
10	0.61	2.94	77
30	0.80	3.43	10

optical transitions (1/2 for direct optical transitions and 2 for indirect transitions).[34,35] As depicted in Figure 2b, two indirect optical band gaps were extracted for the vacuum-deposited device, $E_{g1} = 0.41$ eV and $E_{g2} = 2.76$ eV, implying two distinct optical absorption bands. The observed indirect E_{g1} transition may be attributed to a transition between oxygen vacancy (V_O) states and valence band or conduction band. The value of $E_{g2} = 2.76$ eV is comparable to the band gap of MoO_3 and WO_3, ≈2.7–3.2 eV for MoO_3 or ≈2.7–3.5 eV for WO_3 depending on deposition techniques,[36] implying the association of these elements with V_Os. As indicated in Figure 2c, the Tauc fitting plots of the direct transitions all converge at a single energy regardless of oxygen partial pressure during thin film deposition, implying that the primary direct optical band gap of the HEO film is in the range of 5.35–5.40 eV. For absorption-coefficient values lower than 10^4 cm^{-1}, an exponential bandtail is observed where the Urbach energy (E_U) can be extracted by the formula, $\alpha = \alpha_0 \exp(h\nu/E_U)$, as shown in Figure 2a.[37–39] The Urbach energy in an amorphous material characterizes localized states that may arise from defects or crystalline disorder. Increasing the oxygen partial pressure during thin film deposition increases the optical band gap and decreases Urbach energy, as summarized in **Table 1**. The optical band gap of the HEO associated with Mo and W decreases with oxygen deficiency, which is similar to the case of (Ce, Gd, La, Nd, Pr, Sm, Y) HEO materials.[27] Additionally, the abrupt reduction of Urbach energy for oxygen partial pressure between 10 and 30 mTorr suggests a possible recovery of the crystallinity by oxygen compensation under these thin film deposition conditions.

We also calculated the band gap of amorphous (Zr, Hf, Nb, Ta, Mo, W)-based HEOs as a function of oxygen composition with hybrid density functional theory (DFT) in **Figure 3**a. The calculated band gap for the stoichiometric composition, $(Zr,Hf,Nb,Ta,Mo,W)_2O_5$, is 3.38 eV and is close to the measured indirect E_{g2} for the HEO thin films deposited at the oxygen partial pressure of 30 mTorr. We also calculate the band gaps of amorphous HEO for oxygen-deficient compositions, $(Zr,Hf,Nb,Ta,Mo,W)_2O_{5-x}$, and find a narrowing band gap with increasing oxygen deficiency, x. The calculated band gap for $x = 0.1667$ is comparable to the measured indirect E_{g2} of the vacuum-deposited HEO films, implying off-stoichiometry of our films. Therefore, our calculation results show that the band gap of HEO corresponds to the optically measured gap E_{g2} of the HEO thin films that decreases with decreasing oxygen partial pressure during film deposition, and can be tuned by varying the oxygen stoichiometry.

To further explore the origin of V_O in the HEO thin film, XPS (**Figure 4**) was performed. Detailed information of XPS fitting and decomposed peak positions are presented in Supporting Information, where Zr, Hf, and Ta spectra exhibit good agreement with their binary oxide for the lowest cation oxidation state (ZrO_2, HfO_2, and Ta_2O_5, respectively) as shown in Figure S1, Supporting Information. However, the Nb, Mo, and W XPS spectra exhibit clear suboxide peaks (less than stoichiometric proportion of oxygen, with peaks denoted as Nb^{4+}, Mo^{4+}, Mo^{5+}, and W^{4+} in Figure 4) that vary with oxygen partial pressure. For deposition with 30 mTorr oxygen partial pressure, the Nb^{4+} peaks disappear, the Mo^{4+} peaks decrease, the Mo^{5+} peaks increase, and the W^{4+} peaks strongly decrease. In all cases, suboxide peaks decrease for the 30 mTorr condition, suggesting that V_Os of the (Zr, Hf, Nb, Ta, Mo, W) HEO that originate from Mo and W (and a small amount of Nb) are compensated by the ambient oxygen gas during PLD. However, no distinctive differences were observed in the XPS spectra for the range of oxygen partial pressure from a vacuum to 10 mTorr, consistent with the optical characteristics. The observed oxygen compensation mechanism is further corroborated by the analysis of the cation charge (Bader charge) for the calculated HEO structures (Figure 3b). For the composition of
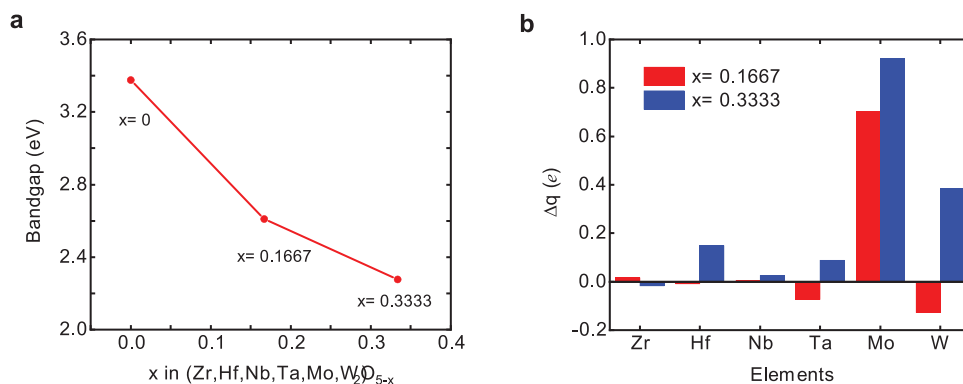

Figure 3. First-principles calculation of HEO thin film. a) The HSE06-calculated band gap of amorphous $(Zr,Hf,Nb,Ta,Mo,W)_2O_{5-x}$ as a function of oxygen deficiency x. The band gaps are quasidirect gaps, that is, indirect gaps that are folded to the gamma point in the alloy supercell. The band gap decreases with increasing oxygen deficiency. b) The change in the Bader charge of the cations in the oxygen deficient amorphous $(Zr,Hf,Nb,Ta,Mo,W)_2O_{5-x}$ alloy compared to the stoichiometric composition. e denotes unit charge. The oxygen deficiency is compensated by the change in the charge state of the cations, mainly Mo and W.
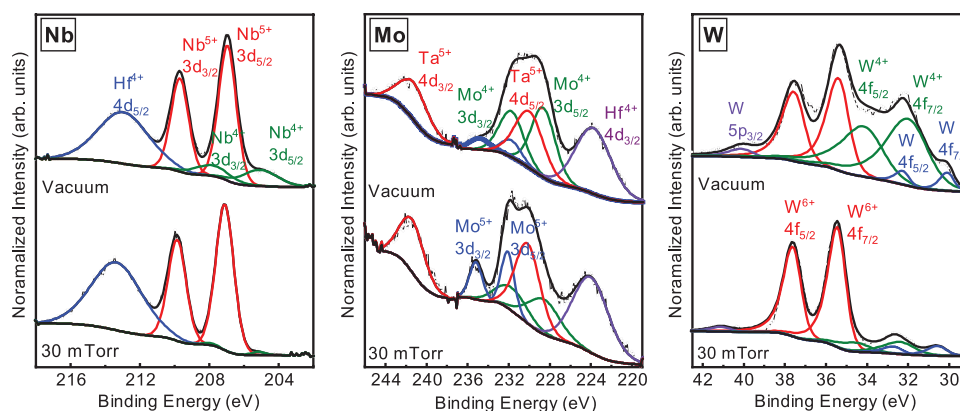
Figure 4. XPS spectra of HEO thin film deposited in a vacuum and in 30 mTorr of oxygen partial pressure. Core level spectra of Nb 3d, Mo 3d, and W 4f are presented. Oxidation states of metal oxide and corresponding decomposed peaks are labeled as same colors.

$x = 0.1667$ in $(Zr,Hf,Nb,Ta,Mo,W)_2O_{5-x}$, the charge state of Mo changes the most (the charge state becomes more negative by $0.7e$ per Mo on average) while the other cations show negligible change in their charge state ($<0.13e$). As the composition gets more oxygen-deficient ($x = 0.3333$), Mo gains more electrons ($0.92e$ per Mo atom) and W also contributes to charge compensation by gaining electrons ($\approx 0.39e$), consistent with our XPS results in Figure 4.

HEO-based memristors were fabricated with the structure shown in Figure 1d,e with their electrical characteristics presented in **Figure 5**. Current-Voltage (I–V) characteristics of the HEO-based memristors deposited under a vacuum condition and a 20 mTorr of oxygen partial pressure are shown in Figure 5a,b, respectively. The I–V curves demonstrate a shift from the high-resistance state (HRS) to the low-resistance state (LRS) during the set process (positive voltage sweep), and a
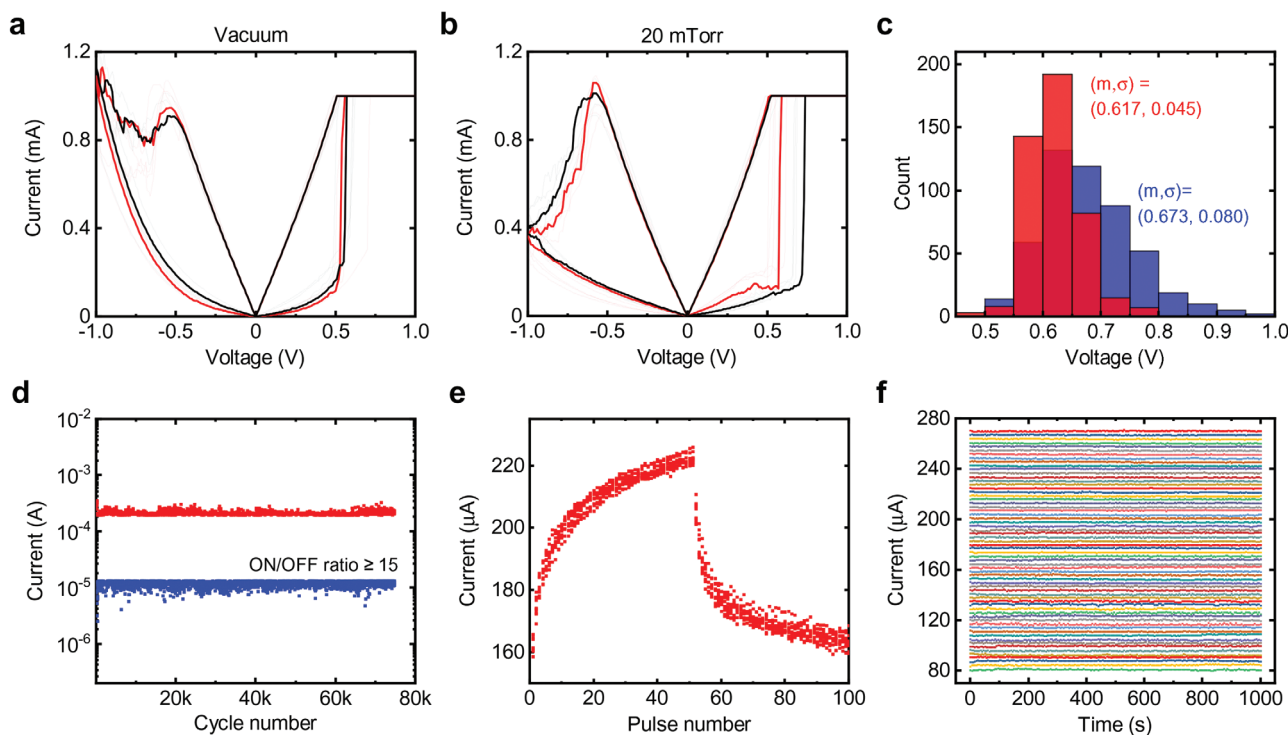

Figure 5. Electric characterization of HEO-based memristors. a,b) Overlapped DC resistive switching of five HEO-based memristors where the film was deposited in a vacuum and in 20 mTorr of oxygen partial pressure, respectively. Forming processes (red) and representative set/reset cycles (black) are depicted. c) A histogram of the set voltages from 10 in-vacuum (red) and 9 in-oxygen (blue) deposited HEO devices (50 cycles per device). The set voltage was defined by the voltage at which the current exceeds a threshold current (0.5 mA) during the positive voltage sweep. Mean (m) and standard deviation (σ) are presented in the figure. d) Endurance test of HEO-based memristors where the film was deposited in 20 mTorr of oxygen partial pressure. e) 10 conductance update cycles of the HEO-based memristor where the film was deposited in a vacuum using 0.8 V/3 µs set pulses, −0.93 V/2 µs reset pulses, and 0.1 V/1 ms read pulses. f) 6-bit operation of HEO-based memristor where the film was deposited in 20 mTorr of oxygen partial pressure. The current level was measured by 0.1 V/1 ms read pulse for every 5 s.

subsequent LRS return to the HRS in the reset process (negative voltage sweep). The resistive switching curves of a reference Ta$_2$O$_{5-x}$ device fabricated with the same device structure are shown in Figure S2c, Supporting Information for comparison. An initial electroforming process typically requires a higher set voltage (referred to as forming voltage) than subsequent set processes, which can severely limit the size of the memristor array and make passive memristor arrays impractical.[40] Moreover, the high forming voltage can increase device variability since stochastically and abruptly generated V_O during the forming process may result in random filament formation inside a switching medium. As shown in Figure 5a,b, both the forming (red) and the set (black) curves indicate a forming-free behavior of these HEO-based memristors, which is desirable for the crossbar array implementations. This forming-free behavior of HEO-based memristors is distinctive in comparison with the reference Ta$_2$O$_{5-x}$ device (Figure S2c, Supporting Information, 1.5 V forming voltage), and HfO$_x$ devices (2 V of forming voltage).[41]

The representative switching curves of five different devices shown in Figure 5a,b exhibit uniform switching behavior, indicating low variability between devices. A low standard deviation (σ = 0.045 V) is observed from the set voltage distribution collected by 500 set/reset cycles with 10 different devices for memristors with the HEO film deposited in a vacuum (Figure 5c, see also Figure S2a,d, Supporting Information for cycle-to-cycle characteristics). Ambient oxygen gas during the HEO deposition influences the variability negatively by increasing a standard deviation (σ = 0.080 V) while the on/off ratio is increased from 6.6 (vacuum) to 13.4 (20 mTorr oxygen) which is attributed to the increased resistance at the HRS. These results imply that the V_O in the HEO was compensated by ambient oxygen gas during the deposition, thereby increasing the electrical resistivity.

HEO-based memristors endured up to 70k of switching cycles (Figure 5d), where the on/off ratio was maintained more than 15 with a write-verify scheme. Open-loop set-reset testing (Figure 5e) shows that the HEO devices offer gradual analog conductance increments and decrements with low variation. In the high temperature retention test (Figure S2f, Supporting Information), HEO-based memristors maintained LRS for more than 20 h at 100 °C. Multi-bit per a single memristor is a desirable characteristic for neuromorphic computing and high-density memory applications.[42] To investigate multi-bit capability, HEO-based memristors where the film was deposited in 20 mTorr of oxygen partial pressure were selected to utilize the larger on/off ratio that is suitable to store many states. 6-bit (64 levels) operation was demonstrated by using the write-verify scheme and following 10^3 s of retention (Figure 5f). The initial voltage for the set and reset pulses are 0.5 V and –0.5 V, respectively. After each programming (set or reset) pulse, the device state is checked in the verify step, where the current is measured by a 0.1 V/1 ms read pulse. If the current is not within ±0.25 µA of the target range, the programming voltage is incremented or decremented by 0.02 V and the device is re-programmed. The feedback loop of the write-verify scheme allows the device to operate in a larger dynamic range, since the set/reset voltage pulse amplitudes can be adjusted based on the device response, whereas the set/reset pulses are fixed in the open-loop operations. For the 6-bit operation, 64 target current levels separated by 3 µA from 81 µA to 270 µA were used. With the write-verify scheme, the device can be programmed to ±0.25 µA of the target levels and maintains within ±1.5 µA of the target current levels, as shown in Figure 5f. Notably, the HEO-based memristors achieved the 6-bit operation without current-limiting transistors or external instruments for current compliance.

3. Discussion

The promising results of (Zr, Hf, Nb, Ta, Mo, W) HEO-based memristors may be attributed to the increased and well-distributed V_O concentration originating from the unique properties of high-entropy materials. V_O in HEO materials can be instantly generated by compensating the charge imbalance between the substituents in an oxygen-deficient environment.[26,27] Furthermore, HEO thin films were intentionally grown in a vacuum at a low substrate temperature (40 °C) in order to achieve an oxygen-deficient amorphous film. The existence of shallow V_O states (0.41 eV), the band gap narrowing with increasing V_O, and the broad Urbach tail, which were verified by optical characteristics and XPS analysis, indicate a high concentration of V_O associated with Mo and W in the HEO films. The uniform distribution of V_O may decrease the stochastic behavior in filament formation, which leads to low variability with forming-free behavior. The resistive-switching characteristics of memristors can be explained by the formation and disruption of filaments and can be described by the V_O continuity equation, the ion hopping model of Mott and Gurney, and Soret diffusion.[28] Figure 1d illustrates the filament formation and disruption processes governed by ionic migration. Soret's diffusion, which depends on a temperature gradient, opposes ionic diffusion described by Fick's law. The observed stable 6-bit operation (Figure 5f) and the long retention at 100 °C (Figure S2f, Supporting Information) may be attributed to the limited V_O diffusion influenced by the sluggish diffusion effect of high entropy materials,[25] balancing these two diffusion processes. Moreover, the characteristics of high-entropy materials offer thermodynamic stability to the device by restraining phase segregation in a switching medium. In the analog conductance update curves of typical memristors, as applying consecutive set pulses, the conductance increases abruptly at first then increases gradually. The first abrupt increase can be interpreted as the sudden connection of two electrodes by filament formation dominated by ion drift, while the subsequent gradual increase results from filament widening due to ion diffusion.[43] The abundant and well-distributed V_O in HEO thin films may reduce the range of filament connection, resulting in the gradual conductance increase as well as the forming-free behavior.

4. Conclusion

In this work, an amorphous (Zr, Hf, Nb, Ta, Mo, W) HEO system was proposed and applied to successfully fabricate memristor devices. The HEO thin films deposited by PLD result in homogeneous films for fundamental exploration of memristor behavior, where future development of production-friendly physical and chemical deposition techniques is needed

**ADVANCED
SCIENCE NEWS**
www.advancedsciencenews.com

**ADVANCED
ELECTRONIC
MATERIALS**
www.advelectronicmat.de

to understand feasibility for practical applications. The HEO thin films demonstrate favorable memristor characteristics for neuromorphic applications by exhibiting low variability, forming-free behavior, gradual conductance modulation, 6-bit operation, and long retention, which are competitive with the existing state of the art memristors. The forming-free and gradual conductance modulation are similar to the results of WO_3-based memristors, while the retention behavior is significantly better than WO_3 and similar to retention advantages offered by HfO_2- and Ta_2O_5-based memristors. These results suggest that the concept of the "cocktail" effect of high-entropy materials is favorable for combining virtues of varying oxide memristor technologies to improve the overall memristor characteristics without the conventional performance trade-offs associated with binary oxide materials alone. Further theoretical guidance and experiments to explore the dependence of oxygen vacancy and filament formation on variable HEO mixtures will serve to guide the search for optimum memristor characteristics. We conclude that HEOs offer unique functionality to overcome material challenges related to the inherent stochastic behavior in memristor development.

5. Experimental Section

PLD Target Preparation: The HEO PLD target was fabricated by SCI Engineered Materials by vacuum hot pressing (600 °C) with equimolar fraction of six transition metal oxide powders (ZrO_2, HfO_2, Nb_2O_5, Ta_2O_5, MoO_3, and WO_3). A sintering temperature of 600 °C was selected to minimize evaporation of MoO_3 (795 °C melting point) and to achieve robust solid target.

Thin Film Deposition by PLD: (Zr, Hf, Nb, Ta, Mo, W) HEO thin films were deposited on thermally grown SiO_2 (100 nm)/Si(100) substrates by PLD at variable oxygen partial pressure to tune resistive switching characteristics. The substrate temperature was set to 40 °C in order to achieve amorphous films to facilitate ionic migration for the memristor switching medium. A KrF excimer laser (248 nm laser wavelength and 10 nm pulse width) was used with laser pulse energy of 300 to 500 mJ and 5 Hz repetition rate. Oxygen partial pressure was adjusted from a vacuum (10^{-5} Torr) to 30 mTorr. Prior to the deposition on the samples, HEO targets were ablated for 1 h under 100 mTorr of oxygen partial pressure. The deposition parameters were controlled to achieve HEO film thickness within the range from 5 to 10 nm. The position of samples on the substrate heater, substrate-target distance, target rotation, and a beam area (0.124 cm^2, adjusted by optics) was fixed for all depositions.

Memristor Fabrication: HEO thin films were deposited on the SiO_2/Si(100) substrates with lithographically patterned Pd (40 nm) bottom electrode deposited by electron beam evaporation. After HEO film deposition by PLD, 30 nm of Ta and 40 nm of Pd were patterned and deposited in sequence for top electrodes with a resulting device area of 2 μm × 2 μm. Magnetron sputtering and electron beam evaporation were used for Ta and Pd layer depositions, respectively. Additional Au pads (700 nm) were similarly deposited to facilitate electrical probing.

Thin Film Characterization: Spectroscopic ellipsometry (Woollam M-2000) was used to characterize the film thickness and investigate optical characteristics of the film. For the ellipsometry fitting, the HEO film was assumed as a Cauchy medium with surface roughness (50% void content) and using the Kramers-Kronig relation. For thick HEO films (>200 nm), surface profilometry (Dektak XT) was used for thickness determination. XRD was performed by the PB-PSA mode (parallel beam with parallel slit analyzer) of a Rigaku Smartlab XRD system at grazing incidence angle ($\omega = 0.5°$) using a Cu Kα_1 X-ray

source. The grazing incidence mode was selected considering the thin film thickness of the HEO film (182 nm, specially prepared for XRD). For EDS mapping, a 660 nm thick HEO film sample was prepared since the depth resolution of EDS was on the order of 1 μm. X-ray photoelectron spectroscopy (XPS, Kratos Axis Ultra XPS system) was performed with 20 eV of pass energy, 0.1 eV of step energy, and sweeping five times. The peak positions of decomposed peaks and their fitting method analyzed by CASA XPS software are listed in Table S1, Supporting Information.

Electrical Characterization: DC resistive switching characteristics were measured by a Keithley 4200-SCS Semiconductor characterization system. Consecutive positive (with 1 mA compliance current) and negative voltage sweeps were applied to the devices for *I–V* measurements. National Instruments USB-6259 multifunction data acquisition device and model 1211 current preamplifier from DL Instruments were used for pulse measurements in Figure 5d–f. For the endurance test (Figure 5d), a write-verify scheme was used with target currents of 200 μA and 13.3 μA (read by a 0.1 V/1 ms pulse) for LRS and HRS states, respectively. The initial set and reset pulse voltage was 0.7 V and −1.2 V for set and reset, respectively. The on/off ratio was maintained larger than 15 during 70k of set/reset cycles. The conductance updates used 50 identical set pulses (0.8 V/3 μs) followed by 50 identical reset pulses (−0.93 V/2 μs) without any feedback (Figure 5e) to examine linearity of conductance behavior. The 6-bit operation data (Figure 5f) used the write-verify scheme discussed in the main text.

Computational Details: To obtain the electronic structure of amorphous (Zr,Hf,Nb,Ta,Mo,W)-based HEOs with varied composition of oxygen, first-principles calculations were performed based on hybrid DFT using the projector augmented wave method,[44,45] and the Heyd–Scuseria–Ernzerhof (HSE06) functional,[46] as implemented in the Vienna Ab initio Simulation Package (VASP).[47–49] The employed pseudopotentials included the Zr $4s^24p^65s^24d^2$, Hf $6s^25d^2$, Nb $4s^24p^65s^24d^3$, Ta $6s^25d^3$, Mo $5s^24d^4$, W $6s^25d^4$, and O $2s^22p^4$ electrons in the valence with a plane-wave cutoff energy of 400 eV. The amorphous (Zr,Hf,Nb,Ta,Mo,W)$_2O_{5-x}$ structure was generated by the melt-and-quench method of ab initio molecular dynamics simulations.[50] The initial cell structure of crystalline (Zr,Hf,Nb,Ta,Mo,W)$_2O_5$ alloy was first modeled with equimolar cation composition using the 42-atom supercell where the alloy randomness was modeled by Special Quasi-random Structures,[51] generated with the Alloy Theoretic Automated Toolkit (ATAT).[52] The initial cell was then annealed at a temperature of 4000 K for 18 ps using a Nose-Hoover thermostat,[53,54] and subsequently cooled down to 1000 K with a cooling rate of 3000 K/12 ps. After the melt-and-quench step, a damped molecular-dynamics simulation was performed to optimize the unit cell shape and atomic positions with a maximal force criterion of 0.02 eV Å^{-1}. For the nonstoichiometric composition, that is, (Zr,Hf,Nb,Ta,Mo,W)$_2O_{4.833}$ and (Zr,Hf,Nb,Ta,Mo,W)$_2O_{4.667}$, oxygen atoms from the initial stoichiometric cell was removed, and the amorphous structures was generated using the molecular dynamics simulations with the same parameters applied for the stoichiometric composition. The final crystal structures of the amorphous (Zr,Hf,Nb,Ta,Mo,W)$_2O_{5-x}$ ($x = 0$, 0.1667, 0.3333) are shown in Figure S3a–c, Supporting Information. The radial distribution function of atomic bonds in Figure S3d, Supporting Information shows the disorder of the atomic geometry. For the obtained amorphous structures of (Zr,Hf,Nb,Ta,Mo,W)$_2O_{5-x}$, hybrid DFT calculation was performed using the HSE06 functional to correct for the underestimated band gap. The amount of Hartree–Fock mixing exchange was set to 25% and a 2 × 2 × 2 Γ-centered Brillouin-zone was used for sampling the k-grids. The charge density was analyzed by using the Bader charge analysis codes to assign the total charge associated with each atom.[55,56]

Supporting Information

Supporting Information is available from the Wiley Online Library or from the author.

**ADVANCED
SCIENCE NEWS**

www.advancedsciencenews.com

**ADVANCED
ELECTRONIC
MATERIALS**

www.advelectronicmat.de

Acknowledgements

Conflict of Interest

The authors declare no conflict of interest.

Data Availability Statement

Data openly available in a public repository that does not issue DOIs.

Keywords

[1] A. Chen, *Solid-State Electron.* **2016**, *125*, 25.

[2] G. C. Adam, A. Khiat, T. Prodromakis, *Nat. Commun.* **2018**, *9*, 5267.

[3] Y. Chen, *IEEE Trans. Electron Devices* **2020**, *67*, 1420.

[4] Y. V. Pershin, M. Di Ventra, *IEEE Trans. Circuits Syst.* **2010**, *57*, 1857.

[5] D. B. Strukov, G. S. Snider, D. R. Stewart, R. S. Williams, *Nature* **2008**, *453*, 80.

[6] A. Mehonic, A. Sebastian, B. Rajendran, O. Simeone, E. Vasilaki, A. J. Kenyon, *Adv. Intell. Syst.* **2020**, *2*, 2000085.

[7] S. H. Jo, T. Chang, I. Ebong, B. B. Bhadviya, P. Mazumder, W. Lu, *Nano Lett.* **2010**, *10*, 1297.

[8] W. Zhang, B. Gao, J. Tang, P. Yao, S. Yu, M. Chang, *Nat. Electron.* **2020**, *3*, 371.

[9] F. Cai, J. M. Correll, S. H. Lee, Y. Lim, V. Bothra, Z. Zhang, M. P. Flynn, W. D. Lu, *Nat. Electron.* **2019**, *2*, 290.

[10] P. Yao, H. Wu, B. Gao, J. Tang, Q. Zhang, W. Zhang, J. J. Yang, H. Qian, *Nature* **2020**, *577*, 641.

[11] A. Serb, J. Bill, A. Khiat, R. Berdan, R. Legenstein, T. Prodromakis, *Nat. Commun.* **2016**, *7*, 12611.

[12] A. Sebastian, M. L Gallo, R. Khaddam-Aljameh, E. Eleftheriou, *Nat. Nanotechnol.* **2020**, *15*, 529.

[13] R. Gharpinde, P. L. Thangkhiew, K. Datta, I. Sengupta, *IEEE Trans. VLSI Syst.* **2017**, *26*, 355.

[14] C. E. Graves, C. Li, X. Sheng, D. Miller, J. Ignowski, L. Kiyama, J. P. Strachan, *Adv. Mater.* **2020**, *32*, 2003437.

[15] Y. Sharma, B. L. Musico, X. Gao, C. Hua, A. F. May, A. Herklotz, A. Rastogi, D. Mandrus, J. Yan, H. N. Lee, M. F. Chisholm, V. Keppens, T. Z. Ward, *Phys. Rev. Mater.* **2018**, *2*, 60404.

[16] Y. Yang, W. Lu, *Nanoscale* **2013**, *5*, 10076.

[17] B. Chakrabarti, M. A. Lastras-Montaño, G. Adam, M. Prezioso, B. Hoskins, M. Payvand, A. Madhavan, A. Ghofrani, L. Theogarajan, K.-T. Cheng, D. B. Strukov, *Sci. Rep.* **2017**, *7*, 42429.

[18] C. M. Rost, E. Sachet, T. Borman, A. Moballegh, E. C. Dickey, D. Hou, J. L. Jones, S. Curtarolo, J.-P. Maria, *Nat. Commun.* **2015**, *6*, 8485.

[19] J. W. Yeh, S. K. Chen, S. J. Lin, J. Y. Gan, T. S. Chin, T. T. Shun, C. H. Tsau, S. Y. Chang, *Adv. Eng. Mater.* **2004**, *6*, 299.

[20] S. Guo, Q. Hu, C. Ng, C. T. Liu, *Intermetallics* **2013**, *41*, 96.

[21] Y. F. Ye, Q. Wang, J. Lu, C. T. Liu, Y. Yang, *Mater. Today* **2016**, *19*, 349.

[22] D. Bérardan, S. Franger, D. Dragoe, A. K. Meena, N. Dragoe, *Phys. Status Solidi RRL* **2016**, *10*, 328.

[23] D. Bérardan, S. Franger, A. K. Meena, N. Dragoe, *J. Mater. Chem. A* **2016**, *4*, 9536.

[24] A. Sarkar, L. Velasco, D. Wang, Q. Wang, G. Talasila, L. de Biasi, C. Kübel, T. Brezesinski, S. S. Bhattacharya, H. Hahn, B. Breitung, *Nat. Commun.* **2018**, *9*, 3400.

[25] J. W. Yeh, *Ann. Chim. - Sci. Mater.* **2006**, *31*, 633.

[26] Z. Rak, C. M. Rost, M. Lim, P. Sarker, C. Toher, S. Curtarolo, J.-P. Maria, D. W. Brenner, *J. Appl. Phys.* **2016**, *120*, 95105.

[27] A. Sarkar, C. Loho, L. Velasco, T. Thomas, S. S. Bhattacharya, H. Hahn, R. Djenadic, *Dalton Trans.* **2017**, *46*, 12167.

[28] S. H. Lee, J. Moon, Y. Jeong, J. Lee, X. Li, H. Wu, W. D. Lu, *ACS Appl. Electron. Mater.* **2020**, *2*, 701.

[29] T. Chang, S. H. Jo, W. Lu, *ACS Nano* **2011**, *5*, 7669.

[30] H. Y. Lee, P. S. Chen, T. Y. Wu, Y. S. Chen, C. C. Wang, P. J. Tzeng, C. H. Lin, F. Chen, C. H. Lien, M.-. Tsai, in 2008 IEEE Int. Electron Devices Meeting, IEEE, Piscataway, NJ **2008**, pp. 1–4.

[31] J. J. Yang, M.-X. Zhang, J. P. Strachan, F. Miao, M. D. Pickett, R. D. Kelley, G. Medeiros-Ribeiro, R. S. Williams, *Appl. Phys. Lett.* **2010**, *97*, 232102.

[32] C. Weiss, M. Rumpel, M. Schnabel, P. Löper, S. Janz, in 28th European Photovoltaic Solar Energy Conf. and Exhibition, Fraunhofer ISE, Freiburg **2013**, pp. 387–391.

[33] A. Weber, R. Remfort, N. Woehrl, W. Assenmacher, S. Schulz, *Thin Solid Films* **2015**, *593*, 44.

[34] J. Tauc, R. Grigorovici, A. Vancu, *Phys. Status Solidi B* **1966**, *15*, 627.

[35] S. El-Rabaie, T. A. Taha, A. A. Higazy, *Phys. B* **2013**, *429*, 1.

[36] C. G. Granqvist, in *Handbook of Inorganic Electrochromic Materials*, Elsevier Science, Amsterdam, **1995**.

[37] F. Urbach, *Phys. Rev.* **1953**, *92*, 1324.

[38] J. Tauc, *Mater. Res. Bull.* **1970**, *5*, 721.

[39] S. Tiwari, N. Khatun, P. Rajput, D. Bhattacharya, S. N. Jha, C.-M. Tseng, S.-W. Liu, S. Biring, S. Sen, *Appl. Phys. A* **2018**, *124*, 609.

[40] M. J. Lee, C. B. Lee, D. Lee, S. R. Lee, M. Chang, J. H. Hur, Y. B. Kim, C. J. Kim, D. H. Seo, S. Seo, U. I. Chung, I. K. Yoo, K. Kim, *Nat. Mater.* **2011**, *10*, 625.

[41] D. Garbin, E. Vianello, O. Bichler, Q. Rafhay, C. Gamrat, G. Ghibaudo, B. DeSalvo, L. Perniola, *IEEE Trans. Electron Devices* **2015**, *62*, 2494.

[42] S. H. Lee, X. Zhu, W. D. Lu, *Nano Res.* **2020**, *13*, 1228.

[43] Y. Jeong, S. Kim, W. D. Lu, *Appl. Phys. Lett.* **2015**, *107*, 173105.

[44] D. Joubert, *Phys. Rev. B: Condens. Matter Mater. Phys.* **1999**, *59*, 1758.

[45] P. E. Blöchl, *Phys. Rev. B* **1994**, *50*, 17953.

[46] J. Heyd, G. E. Scuseria, M. Ernzerhof, *J. Chem. Phys.* **2003**, *118*, 8207.

[47] G. Kresse, J. Furthmüller, *Phys. Rev. B* **1996**, *54*, 11169.

[48] G. Kresse, J. Furthmüller, *Comput. Mater. Sci.* **1996**, *6*, 15.

[49] G. Kresse, J. Hafner, *Phys. Rev. B* **1993**, *47*, 558.

[50] G. Kresse, J. Hafner, *Phys. Rev. B* **1994**, *49*, 14251.

[51] N. Scott Weingarten, E. F. C. Byrd, *Comput. Mater. Sci.* **2015**, *96*, 312.

[52] A. Van De Walle, P. Tiwary, M. De Jong, D. L. Olmsted, M. Asta, A. Dick, D. Shin, Y. Wang, L. Q. Chen, Z. K. Liu, *CALPHAD: Comput. Coupling Phase Diagrams Thermochem.* **2013**, *42*, 13.

[53] W. G. Hoover, *Phys. Rev. A* **1985**, *31*, 1695.

[54] S. Nosé, *Mol. Phys.* **1984**, *52*, 255.

[55] G. Henkelman, A. Arnaldsson, H. Jónsson, *Comput. Mater. Sci.* **2006**, *36*, 354.

[56] M. Yu, D. R. Trinkle, *J. Chem. Phys.* **2011**, *134*, 64111.

[57] J. Towns, T. Cockerill, M. Dahan, I. Foster, K. Gaither, A. Grimshaw, V. Hazlewood, S. Lathrop, D. Lifka, G. D. Peterson, R. Roskies, J. R. Scott, N. Wilkens-Diehr, *Comput. Sci. Eng.* **2014**, *16*, 62.